Sputtering *p*-Type Arsenic-doped Zinc Oxide Thin Films

John Ryan Peterson

A senior thesis submitted to the faculty of
Brigham Young University
in partial fulfillment of the requirements for the degree of

Bachelor of Science

John Colton, Advisor

Department of Physics and Astronomy

Brigham Young University

ABSTRACT

Sputtering p-Type Arsenic-doped Zinc Oxide Thin Films

John Ryan Peterson
Department of Physics and Astronomy, BYU
Bachelor of Science

Zinc oxide is a promising wide band gap semiconductor with applications in high-temperature, radiation-hard devices and ultraviolet optoelectronics. The p-type material, however, has historically been difficult to produce. In this work, p-type zinc oxide films are grown by rf magnetron sputtering on c-sapphire substrates. Arsenic doping is provided by a Zn_3As_2 intermediate layer. Electrical characterization shows that while the conductivity correlates strongly with substrate temperature while sputtering, carrier type is inconsistent for samples grown in similar conditions. Photoluminescence measurements reveal poor optical performance related to deep defects. These defects may explain the n-type conductivity and comparison with previous work suggests future improvements to the growth process.

ACKNOWLEDGMENTS

Contents

List of Figures

Chapter 1

Introduction

Zinc oxide is a promising wide band gap semiconductor, but decades of study have not solved some of the main problems hindering its adoption. Recent progress, however, has renewed interest in the material. This chapter begins with a basic introduction to semiconductors. Then several of the attractive properties of ZnO are explained, followed by a discussion of the main problems hindering its adoption in devices. The chapter finishes with a discussion of several synthesis methods including the one chosen here.

1.1 Characteristics of Zinc Oxide

Electrons in solids have bands of specific allowed energies. Valence electrons—the immobile electrons which form bonds between atoms—have energies in the valence band. Giving these electrons a jolt of energy can kick them across the band gap into the conduction band, where they may move freely around the solid and conduct electricity. This leaves an electron hole in the valence band, which can also move and conduct electricity, similar to how a bubble can move in water. In a conductor, there is no band gap, meaning that at room temperature, there are many electrons in the conduction band flowing through the material. In an insulator, the gap is so large that essentially no

1

electrons leave their bonds. In a semiconductor, however, the band gap is large enough that most electrons are stuck in the valence band but also small enough that a reasonable jolt of energy can kick them into the conduction band where they can conduct electricity.

Electrons transition to the conduction band by absorbing energy, usually through heat or light. The band gap determines a semiconductor's working temperature range; too much heat floods the conduction band with electrons, while very low temperatures prohibit conduction. The larger the band gap, the higher the temperature required to flood the conduction band. The band gap also determines how the semiconductor behaves optically; a narrow band gap semiconductor will absorb most or all of the visible spectrum, whereas a wide band gap semiconductor will be more transparent. Once an electron is excited into the conduction band, it will eventually drop back into the valence band by emitting energy as a photon or phonons (lattice vibrations).

Semiconductors may have direct or indirect band gaps. With direct band gap semiconductors, when E is plotted vs. k (the electron's crystal momentum), the minimum energy of the conduction band is directly above the maximum of the valence band in momentum space; most electrons don't change momentum very much when transitioning between the two bands. Direct transitions typically emit a photon. In indirect band gap semiconductors, the conduction band minimum is offset from the valence band maximum by a difference in momentum; the resulting transitions typically release or absorb phonons, which have can much more momentum than photons.

The width of the band gap is a very important difference between semiconductors. ZnO is a direct gap semiconductor with a wide band gap of 3.37 eV at room temperature, which corresponds to a wavelength of 368 nm. ZnO and other wide band gap semiconductors ($E_{gap} \geq 3$ eV) have several unique characteristics in comparison to the more common semiconductors Si (1.1 eV) and GaAs (1.4 eV). Temperatures above about 100°C are enough to flood the conduction band in silicon with electrons, making silicon-based devices nonfunctional past this threshold. The wider band gap in ZnO means ZnO-based devices would be stable at higher temperatures. Further, silicon's band

gap is low enough that it absorbs all visible light, but ZnO is transparent—it could be used to create circuits or displays on windows and screens [1]. In addition, ZnO light-emitting diodes (LEDs) would be a good source of UV light for medical treatment and scientific research.

Recent work on a similar semiconductor, GaN, led to the 2014 Nobel prize "for the invention of efficient blue light-emitting diodes which has enabled bright and energy-saving white light sources" [2]. Zinc oxide is set to compete with GaN due to its similar band gap (3.37 eV for ZnO vs. 3.39 eV for GaN). However, ZnO has several advantages over GaN. The first is that the exciton binding energy is much higher at 60 meV, vs. 25 meV in GaN. Excitons, which are bound electron-hole pairs, are one of the primary modes of optical emission; since thermal energy at room temperature is 26 meV, this difference in binding energy could lead to more stable excitons, more frequent exciton recombination, and thus more intense optical emission in ZnO. Further, alloying ZnO with Cd or Mg can increase the band gap far beyond GaN, reaching between 3.0 and 4.0 eV for the two alloys respectively [3–5]. And lastly, ZnO has proven to be exceptionally radiation-hard, which is ideal for space applications [6].

1.2   History of Doping in Zinc Oxide

Semiconductors can be doped with extra electrons in the conduction band (*n*-type) or holes in the valence band (*p*-type). For example, in ZnO, replacing a zinc atom with aluminum donates an extra electron, and so the aluminum dopant is called a donor. Since this additional electron is typically not tightly bound, thermal energy easily excites it into the conduction band and the material becomes *n*-type conductive. Similarly, certain dopants called acceptors lack a valence electron, leaving holes which can move through the lattice and make it *p*-type. Creating semiconductor devices usually requires both *p*-type and *n*-type material. For ZnO, the main difficulty lies in finding a reliable, mass-producible *p*-type doping method.

The group V element nitrogen was for many years expected to form an acceptor by simply replacing O atoms. In practice, doping with N has failed to yield reliable *p*-type material. Not only have nitrogen-doped ZnO films shown limited *p*-type conductivity [7], but they have also proven to be unstable, reverting to *n*-type conductivity after a matter of days or weeks [8]. Further, attempts to produce undoped ZnO usually give *n*-type conductivity, showing that *p*-type doping needs to overcome an intrinsic donor population [9, 10]. All of these problems slowed the progress on ZnO for many years.

Other group V elements P, As, and Sb have recently shown more promise as *p*-type dopants using a wide variety of doping methods [11–18]. The focus in this thesis is arsenic doping. With regards to that, metal-organic chemical vapor deposition (MOCVD) with arsine gas (AsH_3) produced *p*-type films when substrate temperatures up to 600°C were used [12]. Pulsed laser deposition (PLD) with ZnO/Zn_3As_2 targets has produced *p*-type films [14] with Si substrates at 450°C. Sputtering has also produced *p*-type As-doped films: some groups mixed ZnO and Zn_3As_2 together to make a single doped sputter target [15–17], while others chose to cosputter ZnO and an arsenic compound from two different targets simultaneously [18, 19]. The substrates used for cosputtering included Si at 700°C [15], Si/SiO_2 at 400°C [16, 18] and 200–500°C [17], and c-plane sapphire at 300°C [19]. However, these studies did not achieve the combination of high dopant concentration, high mobility, reproducibility, lifetime, and ease of manufacturing required for applications, as evidenced by the present lack of ZnO optoelectronic devices.

The arsenic atoms form *p*-type acceptor defects in the ZnO lattice. Acceptors lack a valence electron compared to the original lattice and produce a positively-charged hole. The exact defect structure is still a matter of debate. The simplest proposed model includes arsenic replacing oxygen, which lacks one valence electron and produces a hole [20]. More complicated models include an As_{Zn}-$2V_{Zn}$ defect complex [21]; this explains how the large arsenic atom is able to fit in the lattice and agrees favorably with the experimentally observed shallow defect binding energies [17, 18].

However, later work disagrees with this analysis, reporting that the As_{Zn}-$3V_{Zn}$ is more stable than As_{Zn}-$2V_{Zn}$ and thus more likely to be found, but it forms a very deep acceptor that cannot cause *p*-type conduction [22]. With this in mind, the exact nature of the acceptor complex is not clear. In addition, while the doping method described here is slightly different from those discussed above and may form a different defect, their successes provide the foundation of this work.

1.3   Unique *p*-type Doping Method

Our growth method includes sputtering ZnO onto a Zn_3As_2 layer at temperatures up to 650°C. Limited published work with this method has shown *p*-type conductivity when ZnO films are sputtered at 450°C on top of Zn_3As_2 on fused silica [13]. Our goal here is to identify the best sputter parameters for high-quality and conductive As-doped *p*-type ZnO thin films.

The exact doping mechanism with the Zn_3As_2 layer is not fully understood, but there are some possibilities. The first theory is diffusion. As the ZnO film forms, the high substrate temperature may cause arsenic atoms to diffuse into the existing ZnO lattice, displacing other atoms and forming an acceptor. The atoms must be hot to move through the lattice and displace other atoms. However, it is also possible that arsenic would bind with oxygen during diffusion, forming a stable arsenic oxide. If this compound were to then diffuse out of the crystal, the dopant would be lost.

Another theory is close space vapor transport. Since the substrate is heated, Zn_3As_2 may evaporate into the atmosphere and redeposit with the sputtered material. As the ZnO layer becomes thicker, however, it is unclear exactly how the arsenic could evaporate into the atmosphere; in this case, it may be that only the bottom of the ZnO layer would be p-type. However, previous work with this doping method revealed arsenic doping throughout the ZnO layer, suggesting that it could still be possible (cf. Look et al. [13] Fig. 1).

It is possible that the arsenic is incorporated by a different mechanism altogether which we

cannot currently explain. In addition, the defect complex formed may not be the same as that formed with the other doping methods already discussed. We compare the defect signatures in the photoluminescence spectra below to investigate this possibility.

1.4 Overview

The goal of this project is to determine the best growth and doping parameters, such as sputter temperature, time, power, and gas flow rates, for sputtering conductive *p*-type ZnO thin films. This introduction has explained the motivation behind the project, such as the applications in high-temperature devices and ultraviolet optoelectronics.

In Chapter 2, we discuss the methods used—first, the film growth, including the steps of substrate preparation and ZnO sputtering, and then sputter target preparation and sample annealing. In addition, this chapter includes step-by-step use guides for some of the laboratory equipment for the benefit of future students in the group.

Chapter 3 presents and discusses the results. This includes physical, electrical, and optical film characteristics. Our results show that the best-performing films were sputtered at 75 W power for 30–60 min at 650°C after 2 min of Zn_3As_2 evaporation. However, reproducibility is poor, and the majority of attempts produce *n*-type samples. Several future experiments are then proposed to improve film quality and reproducibility.

Chapter 2

Experimental Methods

In Chapter 1, we explored the motivation behind our ZnO study, namely the attractive electrical and optical properties of ZnO. In this chapter, we explain the methods used to grow the films using our unique deposition method and characterize them electrically and optically. While this includes background information about the methods used, it also includes specific steps related to our equipment for the benefit of future group members.

2.1   Film Growth

2.1.1   Substrate Preparation

The first step in growing a film is choosing a substrate. The substrate is the material on which the film is deposited, and its structure can heavily impact the film's quality. The best crystalline film quality comes when growing on a crystalline substrate that is lattice-matched to the crystal—the atomic spacing of atoms in the substrate is close to the film's atomic spacing. Without lattice matching, the irregular spacing can cause undesirable defects at the boundary between substrate and film, as the film atoms are contorted into abnormal positions. In addition, if the thermal expansion

coefficients of the substrate and film differ, growing films at high temperature can create stress when the materials are cooled.

In this study, glass, fused silica, and c-axis sapphire substrates were tested. Since sapphire is the only crystalline substrate of the three, it is expected to produce the best films and hence is the focus of the study. Unfortunately, the lattice mismatch is still quite large between ZnO and c-axis sapphire (18%), and the thermal expansion of sapphire is over double that of ZnO [23]. In addition, many of the films contain a Zn_3As_2 intermediate layer, the crystallinity of which is currently unknown.

To examine the effects of the Zn_3As_2 doping, films were grown both on bare substrates and substrates with Zn_3As_2 films. These Zn_3As_2 films were first evaporated with the following steps. The process starts by pouring 99.99% purity Zn_3As_2 powder into an alumina or graphite crucible and then placing the crucible in the tungsten basket in the evaporation chamber. After evacuating the chamber to approximately 10^{-6} Torr, the crucible is heated by turning the variable transformer voltage to 60%. At this point, the basket glows orange-yellow. Evaporation lasted two minutes for all samples in this work, after which the voltage is shut off, the vacuum released, and the sample removed.

Another process that allows direct comparison between doped and undoped samples is masking with tape. By placing Kapton tape on one side of the substrate before evaporation, only half of the substrate has a Zn_3As_2 film. This way, during the sputter process, half of the ZnO film will be directly above a Zn_3As_2 layer, allowing doping by diffusion, and half of it will be near to but not directly above the Zn_3As_2, allowing doping by close space vapor transport. These two doping methods can then be tested with exactly the same growth times and temperatures. Since the substrate temperature in the sputter chamber is as high as 650°C, Kapton tape cannot be used during the sputter process. Another common masking method is Sharpie brand permanent markers; unfortunately, metallic silver Sharpie and green Sharpie both proved difficult to remove after sputtering, likely due to the very high sputter temperatures.

2.1.2   Magnetron Sputtering

After the substrate is prepared and the Zn_3As_2 layer added, the next step is to deposit ZnO. The method we used is called rf magnetron sputtering. The ZnO source is a disc with a diameter of 1-in and roughly 0.1-in thick (see Section 2.1.3), called the target. The general procedure is as follows. Once the target is mounted in the sputter head, a power supply applies a high voltage to the sputter head and target. This voltage ionizes Ar gas in the chamber. The Ar ions bombard the target, knocking material off which then travels down to the substrate and forms a film. To improve efficiency, the sputter head contains a large magnet which confines the plasma near the target. Additionally, the applied voltage is actually an oscillating rf signal, which prevents charge buildup on the surface of the target to allow sputtering of insulating materials.

Here are more specific steps regarding operating the sputtering system, a custom Denton unit. First, turn on the water cooling and open the Ar, O_2, and N_2 gas tanks. Next, place the substrate on the substrate heater. Close the lid and evacuate the system to approximately 10^{-6} Torr and leave the vacuum running and open to the chamber. Set the substrate heater to the desired temperature and turn on the high voltage. Next, open the valves on the Ar and O_2 gas tanks, which should both be set to 80 psi for proper flow controller function. If either of the lines had lost pressure before opening the valves, they should be purged by flowing with no voltage on the sputter head for 15 min before sputtering.

The next step is striking a plasma. Turn on the rf sputter power supply to 75 W and turn on the matching network as well. Turn on the flow controllers, which should be set to 80% (80 sccm) for Ar and 20% (10 sccm) for O_2. The difference in flow rate scaling (100% Ar flow is 100 sccm, while 100% O_2 flow is only 50 sccm) is due to the different flow controllers used for each gas. Since the shutoff valves located above the flow controller box are still off, the flow controllers open wide but no gas flows yet. Next, when the shutoff valves are opened, they at first allow much more gas into the chamber than the settings dictate, but then quickly fall to the desired level. This pressure

spike makes it much easier to strike a plasma. At this point, there should be a bright violet plasma visible in front of the sputter head. If so, sputtering is underway, and the user need only wait several minutes until the film has reached the desired thickness.

To shut off the system, turn off the flow controllers and shutoff valves, power down the sputter power supply, and turn off the substrate heater. When it has cooled somewhat, turn off the vacuum system (ensuring that the turbo pump is isolated from the chamber) and the chamber can then be vented and opened. Inside is a reflective, often colorful ZnO film ready for optical and electrical characterization.

2.1.3   Sputter target preparation

Sputter targets are used up over time and periodically require replacing. Targets are typically made from powders; in this work, 99.999% purity ZnO powder from SkySpring Nanomaterials, Inc. was used. The first step in making a sputter target is to prepare the binder, which is a water-based glue that holds the powder together. The specific binder in this work is Duramax B-1000 made by Rohm and Haas. The binder is added to the powder in small increments, mixing thoroughly with the mortar and pestle in between each addition. Once the mixture has reached the proper consistency, no more binder should be added. The consistency should be similar to clay, but not as fluid as toothpaste. A sample of powder during mixing is seen in Fig. 2.1(a).

After this, the existing clumps in the powder mixture should be broken up, using light circular motions with the pestle to avoid pressing it back into clumps. At this point, the powder mixture should only have small granules—no larger than a millimeter in size. Failing to break up large granules could result in large cracks or pores in the pressed target.

Next, the powder needs to be pressed to the proper shape with a metal die. If the target will be fired at approximately 1100°C or lower, then a 1-in steel die may be used. Firing at hotter temperatures can shrink the target, in which case a 2-in die should be used. The die is first cleaned
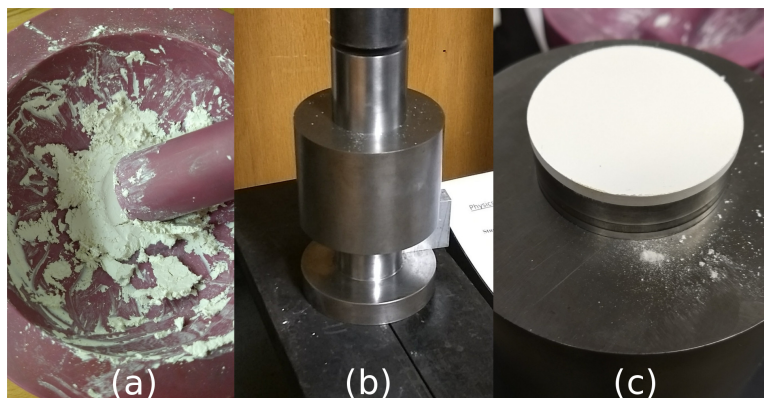
Figure 2.1 Target preparation process including (a) powder during mixing, (b) placement in hydraulic press, and (c) fully formed target ready for firing. Note the rectangular aluminum spacer used in (b) to keep the outer section of the die from falling down.

with oleic acid, and then wiped again with a dry paper towel to remove as much oleic acid as possible. Then, the outer circular die section is placed on the bottom plunger, with a spacer to keep it raised above the inner piston. The powder mixture is poured into the center of the die, and the plunger placed on top. Next, the manual hydraulic press in the student machine shop is used to press the target (see Fig. 2.1b). We found that the best pressure is 3.75 tons for the 2-in die. To read the pressure gauge, note that the ram itself has 3.5-in inner diameter and use the corresponding scale on the gauge. The plunger is removed, followed by sliding the outer circular section down to expose the target for firing (see Fig. 2.1c).

The last step in target preparation is firing, which hardens the pressed powder and removes the binder. Temperatures up to $1100°$C do not change the target size or appearance significantly—after firing, it looks similar to the Fig. 2.1c. However, the nominally 2-in targets are still too large for the sputter head and must be sanded to a 1-in diameter. The belt sander in the main machine shop can do this very quickly. As a reference, the most recent target used 18.15 g of ZnO powder with 4.0 g of binder and produced a 2-in diameter target with a thickness of 0.10 in. This target was then sanded down to a 1-in diameter which is now ready for the sputter chamber.

2.1.4   Annealing

Annealing is a heating and cooling process that can strengthen materials and improve crystal quality. When materials are hot, certain impurities such as dislocations and grain boundaries may work themselves out of the crystal, similar to how a hot iron can remove wrinkles from clothes. In addition, dopant atoms may become mobile and diffuse throughout the crystal. Some effects of annealing can by seen by x-ray diffraction (XRD) studies. These have shown that annealing up to 900°C can significantly improve crystallinity of ZnO films grown on c-sapphire [24].

Annealing may also affect the conductivity as dopants move through the crystal. In one study, annealing sputtered As-doped ZnO on Si at 400°C for 60 min transformed weak *n*-type material to weak *p*-type material [25]. Another study with As-doped ZnO on sapphire found similar results, but with a slightly different annealing method [26]. Some results, however, have shown that annealing can harm films; one group found that annealing As-doped ZnO on silicon at 650°C for longer than 5 minutes actually transformed the *p*-type material into *n*-type material [14]. This suggests that some of these acceptor-forming defects are not thermodynamically stable and annealing could hurt the conductivity. While the doping method and possibly the defect structure of this work differs from those groups, we will need to carefully monitor the effects of annealing to optimize film conductivity.

Samples in this work were annealed at 600 and 700°C in air, and up to 650°C in vacuum. Annealing in air was done in a Thermolyne F6020C-80 furnace; annealing in vacuum, however, was done in the sputter chamber. The maximum safe temperature of the sputter chamber substrate heater is 650°C, but future work will include sputtering in vacuum in a tube furnace at up to 1100°C.

2.2 Film Characterization

2.2.1 Photoluminescence

Photoluminescence (PL) is the process by which an electron is first excited with a photon, and then loses energy by emitting another photon. When the incoming photon has at least the band gap energy of the material, an electron can be excited from the valence band, where it is localized in the bonds, to the conduction band, where it may move throughout the crystal. After excitation, the electron quickly releases thermal energy until it has nearly the minimum energy allowed in the conduction band. Then it eventually returns to the valence band, releasing a photon as it crosses the band gap. In general, measuring the energy of emitted photons allows one to measure the band gap of the material.

When there are additional states within the band gap, the picture becomes more complicated. These are often caused by defects and dopants in the crystal. Electrons can bind with holes to form excitons and lose a small amount of energy in the process. When excitons recombine, the emitted photon will have an energy slightly less than the band gap. In addition, both free electrons and excitons may form bound states with crystal defects and impurities, which gives rise to additional states within the band gap. See Fig. 2.2 for an illustration of these energy levels and optical transitions that could occur.

Ideal donors and acceptors form states very close to the conduction and valence bands respectively. This allows efficient thermal ionization at room temperature to release electrons and holes and increase conduction. In addition, these shallow defects do not significantly reduce PL energy, making good UV emitters. Common emission energies related to defects are donor-bound exciton emission (D^0X), acceptor-bound exciton emission (A^0X), and free-electron-to-acceptor recombination (FA).

Deep states are located midway through the band gap. They are often called traps because it is

Common electronic transitions

Conduction band

D^{0}X

3.4 eV

Zn$_i$ V$_O$

Energy   O$_i$

O$_{Zn}$

A^{0}X

Valence band
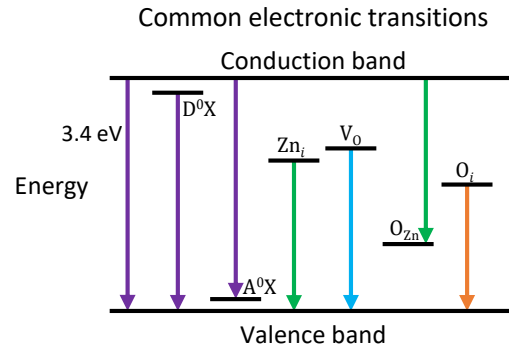
Figure 2.2 Example of energy levels within the band gap, which give rise to the various peaks seen in photoluminescence spectra. The most common shallow defect emission includes the donor-bound exciton D^{0}X and acceptor-bound exciton (A^{0}X), which are related to *n*-type and *p*-type dopants. The undesirable deep emission may come from many sources including poor stoichiometry of Zn and O. The exact levels of these specific deep states are still debated, and this figure is meant only to demonstrate that they emit in the visible range.

very difficult for electrons and holes to escape them. They can reduce conductivity and degrade UV PL performance since recombinations emit much lower photon energies in the visible spectrum. Because a large part of the appeal of ZnO is UV emission, this can be a significant problem. These deep states are demonstrated on the right side of Fig. 2.2.

There are many possible sources of deep defects in the films. The lattice mismatch between ZnO and Zn$_3$As$_2$ or sapphire produces dislocations at the boundary. If the Zn$_3$As$_2$ is polycrystalline or amorphous, this changes the picture as well. Impurities in the target and the chamber gas produce undesirable point defects. Sputtering can also sometimes bombard the substrate heater and/or sputter head, introducing additional impurities.

By comparing our PL spectra with other studies, we may be able to deduce which defects are (or are not) in our films. Significant work has been done to identify which processes are responsible for which emission energies in ZnO, including correlating certain peaks with arsenic acceptors. These are discussed when interpreting the results in Chapter 3.
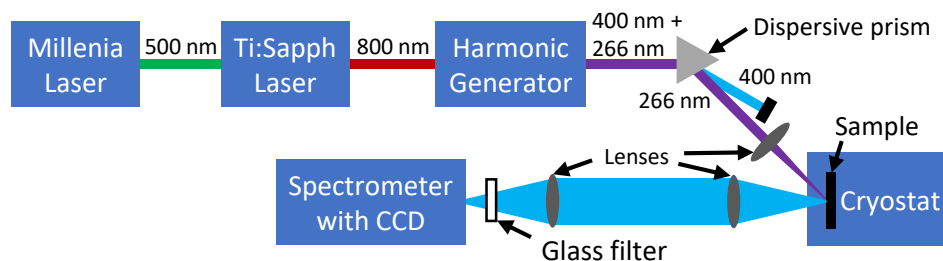
Figure 2.3 Photoluminescence was stimulated with 266 nm light from a frequency-tripled Ti:Sapph laser, and measured with a spectrometer and CCD detector.

2.2.2 Photoluminescence Measurements

Measuring photoluminescence requires exciting the sample with high-energy light. The photons must have greater energy than the band gap energy, which means a wavelength lower than 368 nm for ZnO. In this work, a Spectra-Physics Tsunami titanium-sapphire (Ti:Sapph) laser generated pulsed 800 nm light, which was then frequency-tripled to give 266 nm light. This beam also contains a small amount of frequency-doubled 400 nm light, so we pass it through a dispersive prism to separate the beams. The 266 nm beam then illuminates the sample inside of a cryostat at 16 K. The sample emits PL, which passes through a glass filter to block the scattered 266 nm laser light and is focused into a spectrometer (see Fig. 2.3).

The Ti:Sapph laser works in three stages. First, a Spectra-Physics Millenia XS diode-pumped solid-state laser produces up to 10 W of green 532 nm light in a continuous-wave (CW) beam. This beam is fed directly into the Tsunami titanium-doped sapphire (Ti:Sapph) laser. The green laser light stimulates luminescence in the Ti:Sapph crystal, which in turn emits anywhere in the 700–1080 nm range; however, the laser is tuned to produce one specific wavelength at a time. The knobs on top of the laser allow users to select the wavelength and adjust the pulse length.

The laser must also be mode-locked to use the harmonic generator, meaning that it produces pulses instead of CW light. This can be seen by holding a white paper card in front of the Tsunami output. When the laser is producing CW light, the spot on the card has a fine salt-and-pepper texture

called laser speckle. As soon as the laser is mode-locked, however, the spot on the card appears very smooth. The harmonic generator can then produce frequency-doubled and frequency-tripled light.

Since the laser has a very high infrared peak power of 300 kW, and is also capable of producing deep ultraviolet light, standard optics cannot be used. Fused silica lenses and prisms must be used to steer the beam, since standard BK-7 optics do not transmit far enough into the UV. In this work, 800 nm light from the Ti:Sapph laser is frequency-tripled to produce 266 nm light for PL measurements. Because most filters either do not transmit at 266 nm or can be damaged by the high intensity, we use a nickel-plated slab of fused silica to attenuate the beam to approximately 1% intensity when aligning. Typical beam intensity is 50 mW, so the filter attenuates to a safe level less than 1 mW for aligning.

The PL light is finally focused onto the entrance slit of the JY Horiba TRIAX 550 spectrometer. The spectrometer performs best when the beam is focused using the correct f-number of 6.4, meaning that the distance from the final lens to the slit is 6.4 times the beam diameter at the lens. If the user finds that the spectrometer is miscalibrated, it can be re-calibrated using a Hg lamp as detailed in Appendix A.

The ultraviolet (UV) PL spectra are taken with a single capture of the JY Synapse charge-coupled device (CCD) detector. The visible PL spectra, however, require multiple CCD captures to cover the large spectral range. Since the response across the CCD is not perfectly uniform, stitching together full 39 nm CCD captures yields aliasing with a period of 39 nm. The nonuniformity across the CCD is not significant enough to matter within the single captures used for the UV PL, but does interfere with the multiple captures in visible spectra. Even sampling the spectrum every 5 nm and averaging the multiple captures together gives a very noticeable jagged aliasing pattern with the same spectral period. This can be fixed by sampling every data point at the same locations on the CCD.

One pixel represents about 0.037 nm of spectrum at 370 nm; to avoid having to take an inordinately large number of captures, the pixels on the CCD are binned into groups. In practice

we use bins of approximately 50 pixels, which are about 1.85 nm wide. Then one capture is taken every 1.85 nm through the entire region of interest. Since the spectral density of the pixels varies with wavelength, the bin width is chosen in pixels and then converted to wavelength, and the pixels in every capture are sorted into the bins. This means that bins at higher or lower wavelengths may contain slightly different pixel counts, but this has a negligible effect on the noise level.

Binning multiple pixels together decreases noise, and we can further improve the noise level by using multiple bins per CCD capture. Suppose we want to capture a large spectrum starting at 350 nm using the middle two bins on the CCD. During the first capture, the right bin captures the 350–351.85 nm region of spectrum while the left bin sits idle. Then the spectrometer shifts up by 1.85 nm, and the CCD captures again. This time, the left bin contains the 350–351.85 nm region of spectrum, and the right bin contains the 351.85–353.70 nm region of spectrum. The current left bin is averaged with the previous right bin to give the data point representing 350–351.85 nm, and the current right bin containing 351.85–353.70 nm is saved for the next capture to be averaged with the next left bin. The cycle continues until each data point has been sampled with both the left and the right bins.

The user may specify the number of bins as well as the bin width. In practice, we typically use 10 bins which includes about 50% of the CCD pixels. We avoid the edges of the CCD since features are broadened most in this region; the bins are thus automatically centered around the middle of the CCD. All of the work to bin the pixels, use multiple bins per capture, and raster across the spectral region of interest is done automatically within the software which I wrote.

2.2.3 The Seebeck Effect

The Seebeck effect causes temperature gradients to induce voltages across a semiconductor sample. When a material is heated, the charge carriers (electrons or holes) move faster. If only one part of the material is heated, the charge carriers thermally diffuse away from that part of the material into
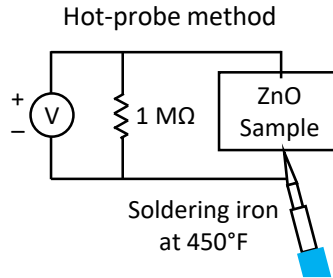
Hot-probe method

Figure 2.4 The Seebeck effect is measured with the hot-probe method. P-type samples produce a negative voltage at the hot probe location as the mobile positive carriers diffuse away. Connecting the voltmeter in reverse as shown will give a positive voltage reading for *p*-type materials and negative voltage reading for *n*-type materials.

the colder region. In a *p*-type film, the charge carriers are holes; when they diffuse away from the hot region, they leave a negative voltage at that region.

2.2.4 Hot-probe Measurements

The hot-probe method uses a soldering iron to measure the Seebeck effect in semiconductor samples. The first step is to connect the negative lead from the voltmeter (Fluke 8840A/AF) to the soldering iron. Then the positive lead is placed on one end of the sample, while the soldering iron (with negative lead attached) is placed approximately 1 cm away. This configuration will yield a positive voltage for *p*-type materials and a negative voltage for *n*-type materials.

If the voltmeter lead is connected directly to the soldering iron with no resistor, the voltage can float when not touching a sample. This can be eliminated by connecting a large resistor ($R \gg R_{\text{film}}$) in parallel with the film. Since most films have resistances on the order of 10^5 Ω or less, a 1 *M*Ω resistor should usually work fine. The experimental setup is depicted in Fig. 2.4.

2.2.5   The Hall Effect

When charges move through a magnetic field, they are deflected by the Lorentz force in the direction perpendicular to both their velocity and the magnetic field. This applies to electric currents in semiconductors too, where it is called the Hall effect. By applying a current across the film in one direction and a magnetic field perpendicular to the film surface, a voltage will arise across the film in the perpendicular direction. In *n*-type and *p*-type semiconductors the carriers are negatively and positively charged, respectively, so the sign of the voltage will correlate with the carrier type.

2.2.6   Hall Measurements

Hall measurements allow accurate measurement of carrier concentration, type, and mobility, as well as sample conductivity. This work used an Ecopia HMS-3000 Hall measurement system to measure carrier type through the Hall effect. The machine features a 0.510 T permanent magnet with sample holder capable of liquid nitrogen cooling to 77 K, or a 1.0 T magnet for room-temperature measurements. This work used only the 0.510 T magnet and only at room temperature.

The sample is mounted using the van der Pauw configuration. This involves four contacts on opposite corners of the sample and allows accurate carrier concentration and type measurements on samples of arbitrary shape (although square is preferable). The sample holder contains four gold contacts to be placed on the four corners of the sample. Instead of applying the current in only one direction, the sample holder cycles through several combinations of these contacts and applies current in several different directions to make directionally-independent measurements. In addition, the machine measured each voltage 1000 times to reduce noise.

Initial tests returned nonreproducible carrier concentrations. Measuring the I-V curves for the samples with the Ecopia software returned nonlinear results. This nonlinear behavior means that the resistance was not constant with regard to applied voltage, and signifies non-ohmic contact between the sample holder and the sample. To make ohmic contact on the sample, we applied solid
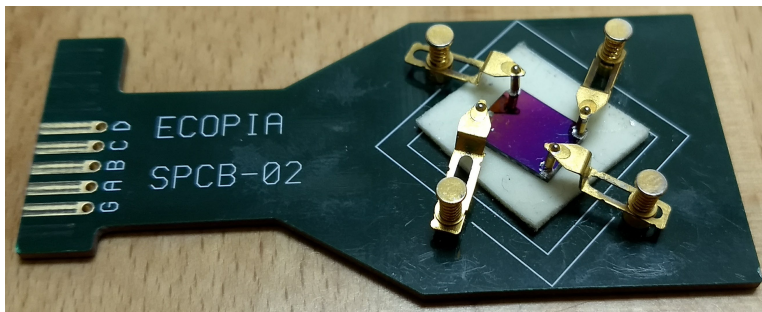
Figure 2.5 A ZnO sample is mounted in the Ecopia HMS-3000 sample holder using the van der Pauw configuration.

indium to each corner. A square sample with indium applied and mounted in the Hall machine sample holder is shown in Fig. 2.5. Next, we verified ohmic contact by measuring the I-V curve up to the same current used for the Hall measurements. Figure 2.6 contains an example of ohmic and non-ohmic I-V curves from the same ZnO sample. In addition, the figure also demonstrates that operating at very low currents (<10 nA) gives unreliable behavior.

Unfortunately, the samples grown on a quarter of a sapphire wafer are too large to fit in the hall device. These can be broken by scoring, but scoring sapphire has proven difficult and many samples break into irregular shapes. Because of this, only a few samples have been tested in the HMS-3000. In the future, we will use a diamond saw to cut all samples to approximately the same dimensions for Hall measurements, and will characterize all samples with the Hall machine.
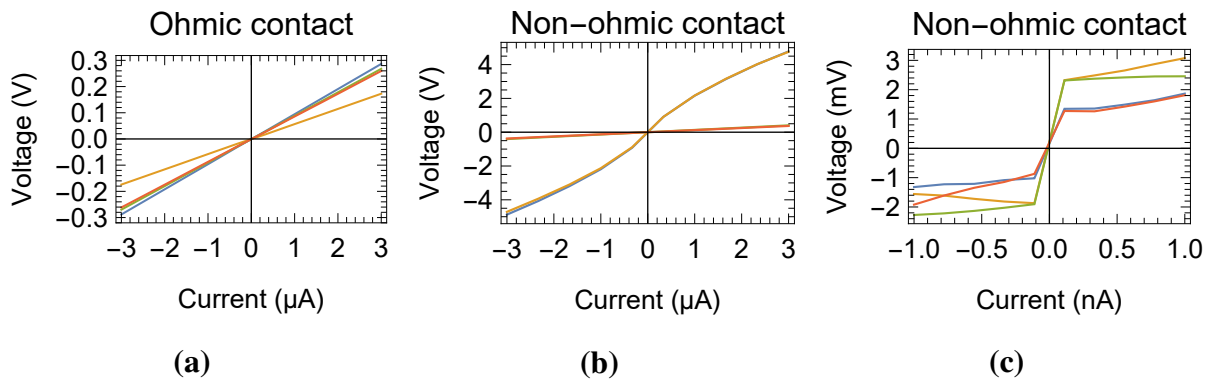
Figure 2.6 Comparison of I-V curves from (a) ohmic contact using indium and (b) non-ohmic contact without indium on one particular ZnO sample. Also included is (c) a more resistive sample showing nonlinear behavior at very low currents. Four contacts are placed on each sample and the different lines on each plot show voltages between neighboring pairs of contacts. The voltages in (a) are very linear, signifying good contact. The voltages in (b) are nonlinear, and in addition the voltage magnitude varies greatly between pairs of contacts. Both of these findings signify poor, non-ohmic contact in (b). The very low current in (c) coupled with the poor contacts yields very erratic and unreliable results.

Chapter 3

Results and Conclusions

In this chapter, we discuss the physical, electrical, and optical results. A few films show occasional *p*-type behavior, but most films grown were *n*-type. The optical results reveal information about some impurities and help point the way for future experiments to reduce unwanted deep defects and increase shallow acceptor defects.

3.1   Physical Properties

The physical properties include the film homogeneity, thickness, and color. The most basic films are ZnO-sapphire films, which are clear as shown in Fig. 3.1 (a). These films also do not change appearance at all when annealed, whether the annealing is done in atmosphere at 700°C or in vacuum at 650°C.

The films containing a Zn_3As_2 layer are reflective. When the Zn_3As_2 layer is first evaporated onto the substrate, it appears silvery as seen in Fig. 3.1 (b). This film is mostly homogeneous, although evaporation frequently leaves large particles on the surface; some can be blown off with compressed air and some cannot. In addition, some Zn_3As_2 films were porous and had many small holes less than a millimeter in diameter. Lower voltage on the variable transformer may slow down
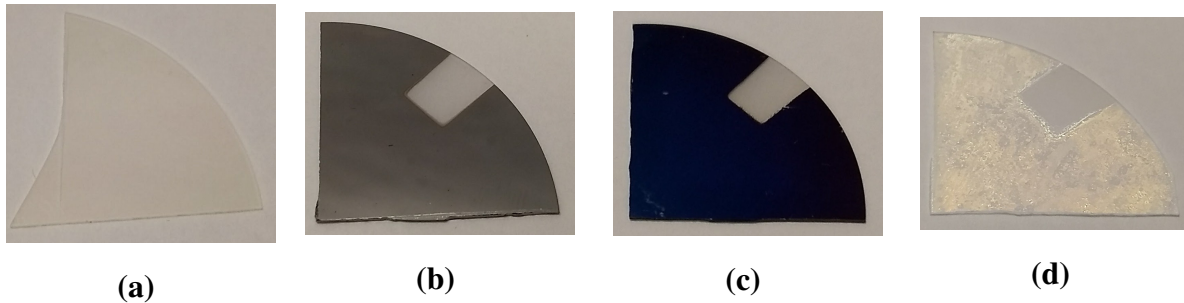
Figure 3.1 Comparison of (a) ZnO-sapphire, (b) Zn_3As_2-sapphire, (c) ZnO-Zn_3As_2-sapphire, and (d) ZnO-Zn_3As_2-sapphire annealed at 700°C in air. The translucent color and rough texture of (d) show that annealing has damaged the film.

the evaporation and allow more uniform deposition.

When a ZnO film is evaporated on top of a Zn_3As_2 film on sapphire, it typically becomes colorful from interference effects. This can be seen slightly in Fig. 3.1 (c), which is dark blue; the colors are more easily seen in person. Most films were sputtered for 30 min and are either yellow or blue. If the sample is only sputtered for a few minutes, the ZnO film will not be thick enough to produce interference effects and it will not change color.

Annealing the ZnO-Zn_3As_2-sapphire films in air at 700°C damaged the films, as seen by comparing Fig. 3.1 (c) (unannealed) and Fig. 3.1 (d) (annealed). These films changed from smooth and reflective to coarse and translucent. It seems that the Zn_3As_2 layer has somehow escaped and broken up the ZnO layer during its exit. The same film damage was seen when annealing in air at 600°C, however, annealing in vacuum at 650°C did not damage the films. With this in mind, it seems that the oxygen in the atmosphere could be responsible; it may have reacted with the Zn_3As_2 layer as it left the film, although further testing is necessary to confirm this.

Film thickness is another important metric. Ellipsometry is a measurement technique that uses the reflection of polarized light to determine sample thickness. Interpreting the reflected intensities requires modeling the data with various functions and can be very difficult. While ellipsometry has only been conducted on a handful of samples thus far, the results are promising. Current models

estimate the thickness of the Zn_3As_2 films between 1 and 2 μm and the thickness of the ZnO films between 100 and 500 nm.

3.2 Electrical Properties

The electrical properties are perhaps the most important, as the goal is to grow *p*-type films. A variety of sputter times and temperatures were tested to optimize for *p*-type films. All undoped ZnO-sapphire films remained insulating as tested by a Fluke 8840A/AF multimeter, and the high resistivity prevented use of the HMS-3000 (e.g., Sample 8 in Table 3.2). Doped samples, that is samples with a Zn_3As_2 layer, reveal a mix of *n*-type and *p*-type crystals as tested by the hot-probe and Hall methods (see Tables 3.2, 3.3).

Electrical tests ruled out close space vapor transport as a viable doping mechanism in our samples. While the ZnO-Zn_3As_2 films were usually conductive, every ZnO film without a Zn_3As_2 layer directly underneath remained insulating. This includes films grown on two halves of the same wafer and adjacent wafers and is shown in Table 3.1 Samples 1 and 2. Further evidence came when measuring the conductivity of the film with a multimeter. When one probe was placed in the the ZnO-Zn_3As_2 region and another slid from the the edge of the ZnO-Zn_3As_2 region into the ZnO-only region, it immediately showed resistive behavior when the probe crossed into the ZnO-only region. This suggests that the arsenic can not travel significant distances through the atmosphere to incorporate into neighboring ZnO regions.

The majority of films with a Zn_3As_2 layer were *n*-type or insulating, although a select few were *p*-type. The annealing tests performed in air at 700°C turned all conductive samples resistive, as shown in Table 3.1, corresponding to the visible physical damage discussed above in Fig. 3.1. While the ZnO-only films were not visibly damaged, they were all insulating before annealing and remained so after.

Table 3.1 Comparison of ZnO doping methods with and without annealing. Samples were deposited on sapphire at 575°C substrate temperature and annealing was done in air at 700°C. Samples were sputtered for 30 minutes with 75 W sputter power. Conductivity type was measured with the hot-probe method.

Sample	No.	Date	Annealed	Type	UV PL (10^3 counts/sec)
ZnO near Zn_3As_2	1	9-7-17	No	insulating	0.925
ZnO near Zn_3As_2	2	9-7-17	Yes	insulating	11.2
ZnO on Zn_3As_2	3	9-7-17	No	*n*-type	1.68
ZnO on Zn_3As_2	4	9-7-17	Yes	insulating	53.0

Film resistance was generally correlated with sample temperature during sputtering, as shown in Table 3.2. While this table only includes a few samples, the trend was seen across dozens of other samples as well. Unfortunately, the carrier type was not reliably correlated with temperature, with only a few samples turning out *p*-type (see Samples 11 and 14 in Table 3.3). Repeatability was poor; two attempts to reproduce samples in Table 3.3 gave slightly different results. The attempt to repeat Sample 9 by making Sample 10 resulted in a much higher resistivity on the second try. The other attempt, with Samples 11, 12, and 13, first gave a partially *p*-type sample, but then gave a uniformly *n*-type sample on the second and third tries along with higher resistivities. During the last attempt (Sample 13), care was taken to purge all possible N_2 from the O_2 line before sputtering to avoid any N_2 contamination. This may account for some difference in resistivity, but further testing is needed to verify this. All of these findings together suggest that there are other factors affecting the doping which have not been accounted for; possible factors are discussed in Section 3.5.

The mixed-type sample in Table 3.3 is a curious case. Half of the sample was *n*-type with both conductivity tests. The other half, however, returned *n*-type with Hall measurements and *p*-type with hot-probe measurements. This contradiction between Hall and hot-probe measurements has been seen in amorphous semiconductors and in semiconductors with inhomogeneous carrier

Table 3.2 Comparison of electrical properties of samples sputtered on sapphire for 30 minutes at various temperatures. Resistances above 10MΩ are listed as infinite. Note that the undoped sample is resistive, but the As-doped samples show correlation between sputter temperature and resistivity.

Sample	No.	Date	Sputter Temp	Type	Resistance across 1 cm
ZnO on Zn_3As_2	5	2-17-18	300°C	insulating	infinite
ZnO on Zn_3As_2	6	2-14-18	500°C	*n*-type	2.5 MΩ
ZnO on Zn_3As_2	7	2-14-18	650°C	*n*-type	10 kΩ
ZnO	8	2-14-18	650°C	insulating	infinite

Table 3.3 Comparison of electrical properties of samples sputtered on sapphire for various times at 650°C. Note that attempts to reproduce the 10-minute and 30-minute samples resulted in significantly different resistances.

| Sample	No.	Date	Sputter Time	Type	Resistance across 1 cm
ZnO on Zn_3As_2	9	2-17-18	10 min	*n*-type	60 kΩ
ZnO on Zn_3As_2	10	2-28-18	10 min	*n*-type	1.0 MΩ
ZnO on Zn_3As_2	11	11-16-17	30 min	mixed	4.5 kΩ
ZnO on Zn_3As_2	12	2-14-18	30 min	*n*-type	10 kΩ
ZnO on Zn_3As_2	13	3-21-18	30 min	*n*-type	55 kΩ
ZnO on Zn_3As_2	14	2-17-18	60 min	*p*-type	400 Ω

concentrations [27]. This particular sample was clearly inhomogeneous, as another piece from the same sample appeared *n*-type in the hot-probe test. In addition, the hot-probe method is a static test, meaning that charges have reached equilibrium and are not flowing during the test. The Hall effect, in contrast, is measured with moving charges and therefore depends on a extra factor of the carrier mobilities. If both carriers are present in comparable concentrations but have different mobilities, the Hall effect may yield an opposite carrier type compared to the hot-probe method.

There is a chance that the Zn_3As_2 layer itself is responsible for the *p*-type conduction. A recent test showed that while the Zn_3As_2 layer is insulating after it is first evaporated onto the sapphire, it becomes slightly conductive and *p*-type when annealed at $650°C$ in the sputter chamber. Since the majority of the sputtered films were grown at $650°C$, the Zn_3As_2 layer in these films is probably conductive. However, the test returned a resistance of about 1 MΩ across 1 cm, which is much higher than the majority of our samples in Tables 3.2 and 3.3, suggesting that it may not affect the sample conductivity very much. Nevertheless, future work should include additional tests to more rigorously study the effects of the Zn_3As_2 layer.

3.3   Photoluminescence

Samples emit photoluminescence (PL) over a large energy spectrum below the band gap. Figure 3.2 demonstrates the natural division between ultraviolet (UV) PL and visible PL. Studying emission in these regions separately provides different information about the sample quality and structure; emission in the UV region corresponds to shallow defect states (including desirable acceptor defects), while emission in the visible region comes from undesirable deep states. These are analyzed separately in Sections 3.3.1 and 3.3.2, respectively.

(a)
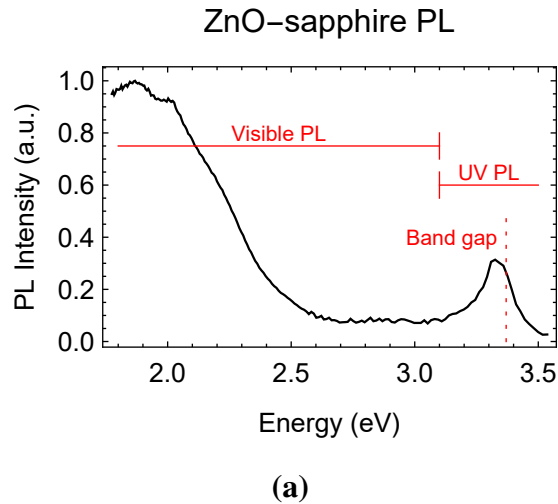
Figure 3.2 Samples emit photoluminescence in the visible (E < 3.1 eV) and ultraviolet (E > 3.1 eV) regions. These regions provide information about the desirable, shallow defects and undesirable, deep defects, respectively. This particular sample, Table 3.1 Sample 1, is discussed further below.

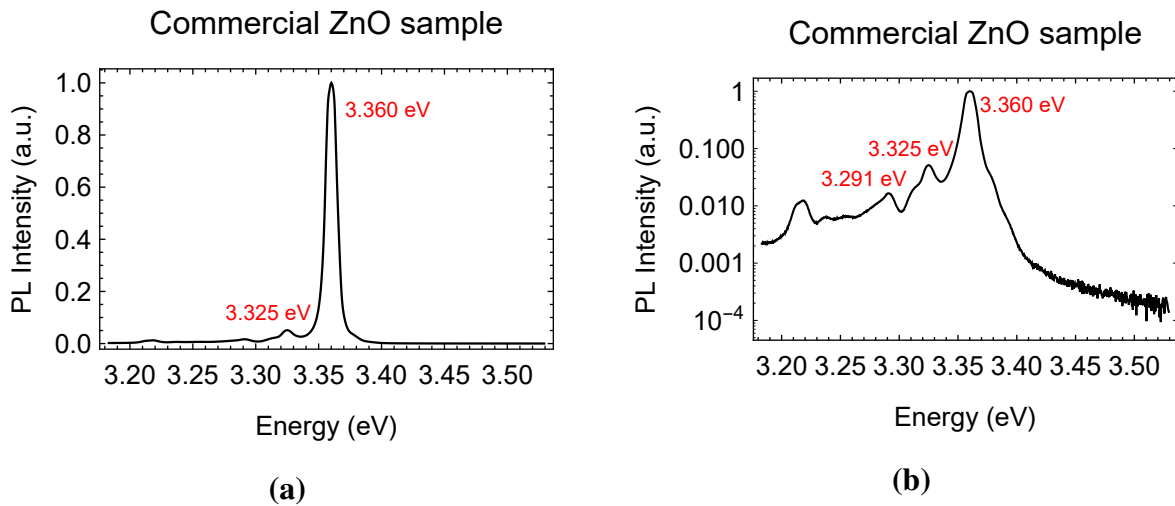### 3.3.1 Ultraviolet Photoluminescence

Ultraviolet photoluminescence (UV PL) can provide important information about crystal structure, dopants, and quality. Photoluminescence from ZnO-sapphire and ZnO-Zn_3As_2-sapphire films generally showed broad, low-intensity UV emission (see Fig. 3.3). These samples have peak widths of approximately 0.1 eV. The location on the sample where PL is measured can impact the results, so these spectra were taken in the center of the film to represent the majority of the sample; edge PL and other anomalous PL is discussed below.

As a comparison, we also measured PL from a commercial *n*-type ZnO sample made by Cermet Inc. The sample is a square, single-crystal wafer with 1-cm edge length and a thickness of 0.5 mm. While this is thicker than our films, our films absorbed all of the laser light, so thickness should not be a factor when comparing PL magnitude to our samples. The PL for this commercial sample is shown in Fig. 3.4.

The PL from the Cermet Inc. sample in Fig. 3.4 shows much narrower peak width (approximately
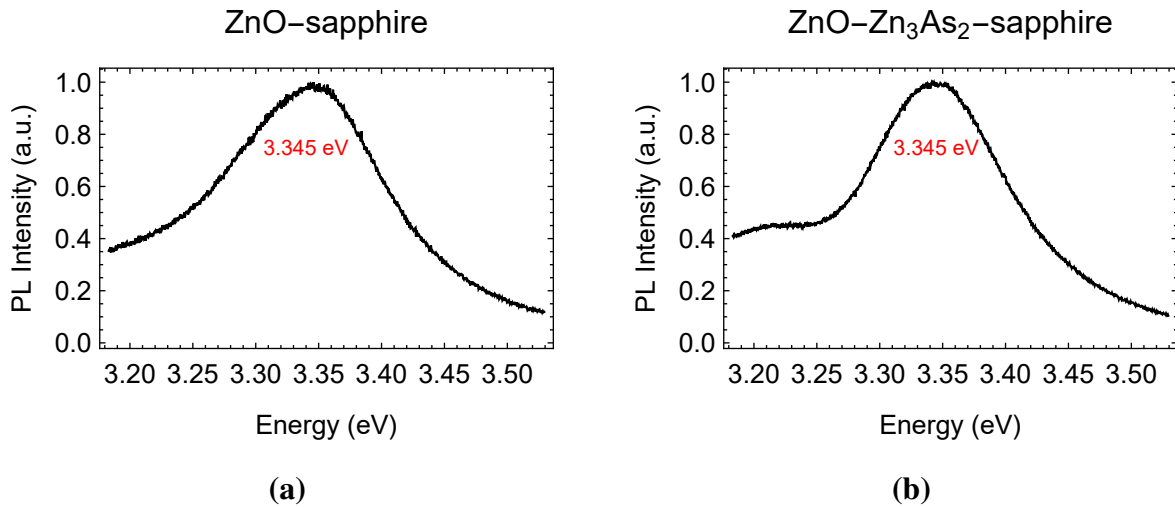
Figure 3.3 Normalized ultraviolet photoluminescence spectra at 16 K of (a) Table 3.1 Sample 1, ZnO-sapphire film and (b) Table 3.1 Sample 3, ZnO-Zn$_3$As$_2$-sapphire film. Peak emission energies are shown in red.
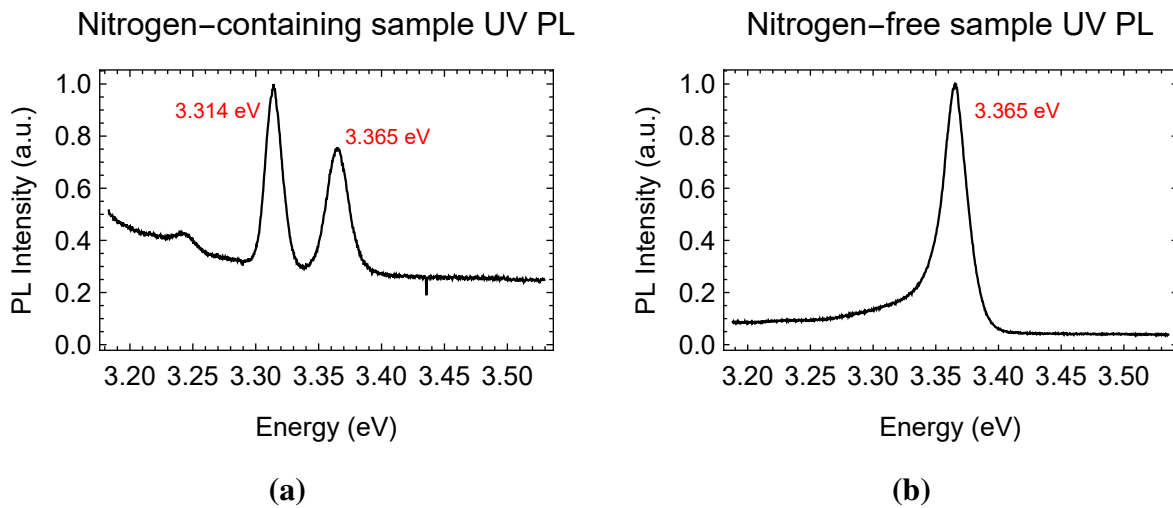

Figure 3.4 Normalized ultraviolet photoluminescence spectra at 16 K of Cermet Inc. *n*-type ZnO wafer with (a) linear and (b) logarithmic scales. Peak emission energies are shown in red.

1/10 the width) than either of the ZnO-sapphire samples in Fig. 3.3, indicating much higher crystal quality. In addition, the emission was much more intense—the plots here are normalized, but in reality the Cermet Inc. sample emits more than 100 times the amount of UV PL (integrated through the UV region) than the unannealed ZnO-sapphire or ZnO-Zn_3As_2-sapphire films. While differences in optical alignment and laser power could account for a small increase, this large of a difference means that the crystal quality of our thin films is far less than the commercial sample.

Photoluminescence spectra also revealed inhomogeneous deposition. Most spots on typical samples showed UV emission similar to the plots in Fig. 3.3. Peaks much narrower and more intense than the average often appeared on the edges of the samples and occasionally on isolated points in the bulk. Intense, narrow-linewidth UV emission signifies better crystal quality. It may be that the film is thinner near the edges, allowing it to grow more epitaxially (more crystalline). The thinnest film grown, however, showed merely average PL linewidth and intensity (see Fig. 3.6), so there may be another explanation.

Locations with more intense UV PL allow us to more directly characterize the impurities. Ideally, the UV PL spectra would show A^0X peaks related to the arsenic doping, confirming that the As is incorporated into the ZnO during deposition and refuting the possibility of a conductive Zn_3As_2 layer. While some spectra showed a 3.314 eV peak that we originally thought to be arsenic-related, later testing showed that the peak occurred in both As-doped and undoped films. We later identified this 3.314 eV peak as nitrogen A^0X emission, in agreement with previous work [7]. Spectra of nitrogen-contaminated and nitrogen-free films are shown in Fig. 3.5.

The cause of the nitrogen contamination was N_2 gas that had diffused into the oxygen supply line. Between sputter sessions, the line had lost pressure and atmospheric N_2 entered. Mass spectrometry with a residual gas analyzer confirmed that when the O_2 supply was first turned on, much more N_2 came into the chamber than O_2. Waiting for 15 minutes with the O_2 flow on was sufficient to purge the N_2 from the line, as shown in the PL peaks (Fig. 3.5(b)).
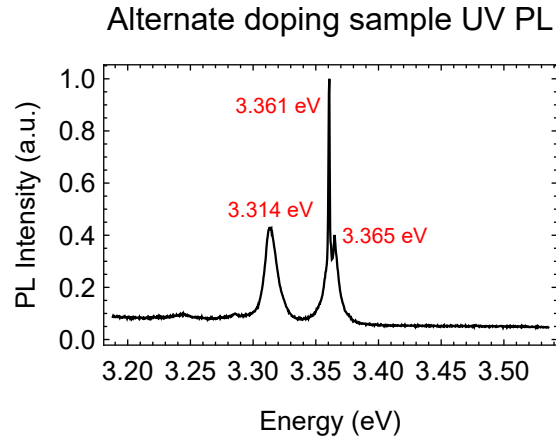
Figure 3.5 Normalized ultraviolet photoluminescence spectra of ZnO film on sapphire at 16 K. Part (a) is Table 3.2 Sample 8 and contains nitrogen impurities, and part (b) has the same growth conditions as Table 3.2 Sample 8 but is nitrogen-free. The presence of the 3.314 eV A^0X peak confirms nitrogen content [7]. Peak emission energies are shown in red, and the spectra were taken at points on the sample showing maximum UV emission. These samples are similar to Table 3.1 Sample 1, whose PL is shown in Figs. 3.3 (a) and 3.7 (a), but with a different growth temperature.

The 3.365 eV peak in Fig. 3.5 is almost certainly donor-related D^0X emission. Previous work found peaks in undoped ZnO spectra at 3.360, 3.364, and 3.367 eV which were identified as donor-bound excitons [28]. Another study found similar peaks at 3.3598, 3.3606, 3.3629, and 3.3568 eV likely from D^0X emission [7]. The 3.3629 eV peak in particular was confirmed as D^0X emission as it has a two-electron satellite feature at 3.3332 eV [7]. These are all very close to the 3.365 eV peak seen in our samples in Fig. 3.5.

It may be possible that our doping method creates a unique defect from that seen in other works, however, it is still instructive to compare with the reported arsenic-related emission energies in the literature. Several groups have proposed A^0X peaks just below the D^0X peaks seen in our films. One group's PLD-grown films showed 3.354 eV As-related emission [26], while another group's MBE-grown samples on GaAs substrates showed 3.355 eV As-related emission [29]. Yet another study identified an arsenic A^0X peak at 3.359 eV [9]. While one group did explain this 3.355 eV peak as D^0X emission [17], the majority of studies agree that this is likely As-related A^0X emission.

There are other possible emission peaks related to arsenic. Excitonic emission could include A^0X emission at 3.337 eV [17] or 3.318–3.328 eV [12]. Alternative FA emission energies could be at 3.282 eV [17], 3.322 and 3.273 eV [9], 3.29–3.31 eV [12], or 3.327 eV [19]. Lastly, emission peaks at 3.260 eV and 3.187 eV have been tied to donor-acceptor pair (DAP) emission and the DAP phonon replica, respectively [19].

Unfortunately, none of the many proposed arsenic-related peaks were consistently seen in our ZnO films. Although we initially measured an intense peak at 3.355 eV, after recalibrating the spectrometer this peak turned out to be D^0X at 3.361 eV. To more directly compare our work with that of other groups, we synthesized one sample using the cosputtering method, where ZnO and Zn_3As_2 are sputtered at the same time [15–19]. This was done by evaporating a thin pie-shaped slice of Zn_3As_2 onto the 1% of the surface area of the ZnO target—ideally yielding 1% As doping in the film. Unfortunately, the target lasted only 2.5 minutes before the Zn_3As_2 had worn through,

Alternate doping sample UV PL

Figure 3.6 Normalized ultraviolet photoluminescence spectrum of sample which was grown with the alternative doping method and is not listed in the tables above. This sputter target used for this sample contained both ZnO and Zn_3As_2 during deposition onto a bare sapphire wafer. The sample was sputtered for only 2.5 min due to the small amount of Zn_3As_2 on the target, and the spectrum was taken at a location on the sample showing maximum UV emission.

resulting in a very thin film. The resulting PL is shown in Fig. 3.6.

The cosputtered sample PL in Fig. 3.6 is largely similar to Fig. 3.5(a) as we had not yet fixed the nitrogen leak when this sample was made. However, what first appeared to be a single D^0X peak is seen here to resolve into two separate D^0X peaks at 3.361 and 3.365 eV. Resolving this second peak was possible because the spectrometer and CCD detector were recently recalibrated (see Appendix A), improving resolution and accuracy to approximately 1 meV. Unfortunately, this sample did not show any of the characteristic arsenic-related PL peaks listed in the literature and was not conductive. It seems likely, then, that the sample quality is not linked to our doping method, but rather with our deposition process itself. In the next section, the visible PL results shed more light on crystal quality.
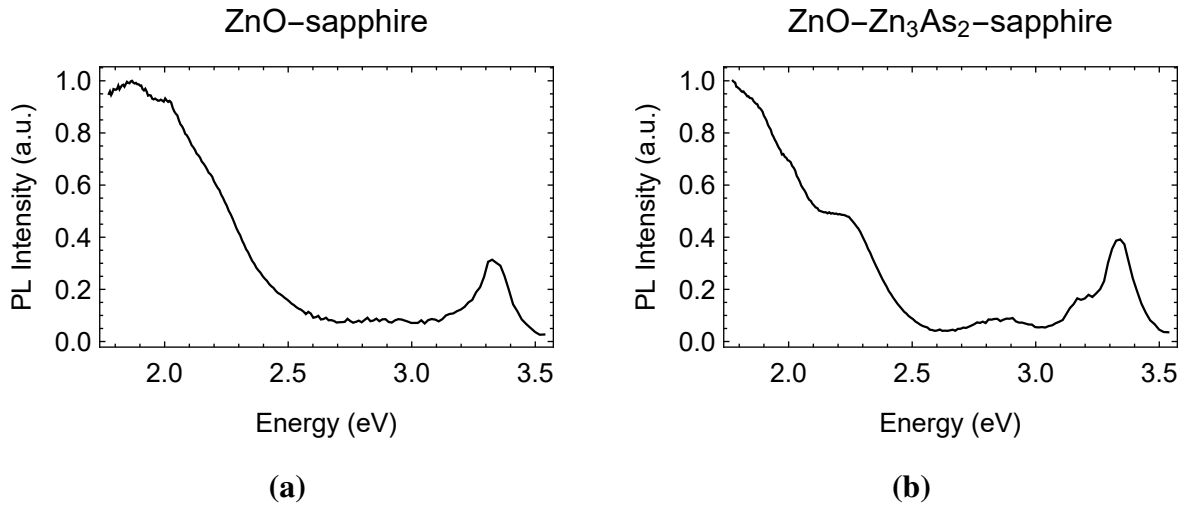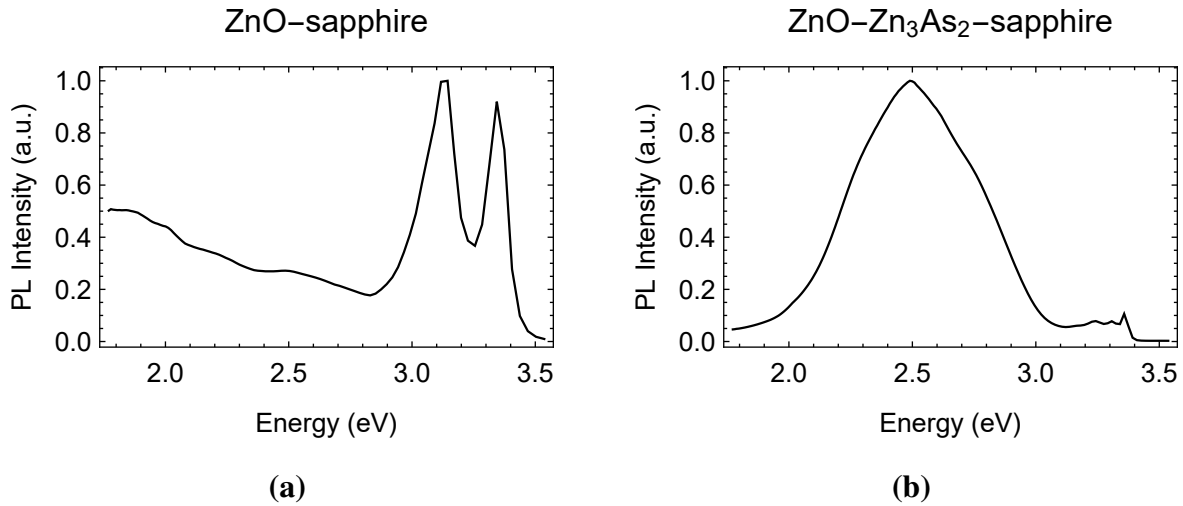
Figure 3.7 Normalized photoluminescence spectra at 16 K of (a) Table 3.1 Sample 1, ZnO-sapphire film and (b) Table 3.1 Sample 3, ZnO-Zn$_3$As$_2$-sapphire film. These are the same samples as in Fig. 3.3.

3.3.2   Visible Photoluminescence

Visible PL (approximately $E < 3$ eV) comes from undesirable deep-level crystal defects. All of the samples showed intense visible emission. Unlike the UV emission, the magnitude of the visible emission remained relatively constant across each sample and did not change spectral shape significantly. Visible PL spectra from the samples used for Fig. 3.3 are reported in Fig. 3.7.

The visible PL in Fig. 3.7 is much stronger than the UV band-edge emission plotted for the same samples in Fig. 3.3. This can also be seen for the sample shown in Fig. 3.2. This indicates a large number of point defects, and could indicate poor crystallinity as well. Annealing is one possible method to improve crystallinity and reduce defects, thus we annealed these films in air at 700°C. The annealed results are shown in Fig. 3.8.

Spectra in Fig. 3.8 show that the Zn$_3$As$_2$ layer strongly affects post-annealing PL when annealed in atmosphere. In the undoped sample (Fig. 3.8 (a)), annealing increased the UV PL peak intensity to about 12 times the unannealed peak intensity (see Table 3.1), while the visible PL intensity only slightly increased; the post-anneal max visible PL intensity is much less than the max UV

ZnO–sapphire

ZnO–Zn$_3$As$_2$–sapphire

(a)

(b)

Figure 3.8 Normalized photoluminescence spectra at 16 K of (a) Table 3.1 Sample 2, annealed ZnO-sapphire film and (b) Table 3.1 Sample 4, annealed ZnO-Zn$_3$As$_2$-sapphire film. These are the annealed versions of the samples in Fig. 3.7.

PL intensity. The origin of the second UV peak which appeared is unknown. The strong UV PL enhancement and less relative visible PL signifies increased crystallinity and/or lower defect count. The story changes, however, with the ZnO-Zn$_3$As$_2$ sample. This sample showed about 32 times higher UV PL intensity after annealing (see Table 3.1), but the post-anneal PL spectrum (see Fig. 3.8 (b)) shows that the visible PL intensity is now much higher than the UV PL, meaning that the visible PL has increased by at least a factor of 100. This very high visible emission signifies high defect count and correlates with the film damage seen after annealing in Fig. 3.1. The exact defects causing the visible PL are not known, but the fact that they are deep in the band gap is not good for electrical performance.

One possible defect source is the lattice mismatch. However, other groups have obtained very high-quality PL with various deposition methods on the same substrate. Undoped molecular beam epitaxy (MBE) ZnO films on c-plane sapphire have achieved 2000 times higher UV PL intensity relative to visible PL intensity when grown at 600°C [23]. Another group demonstrated phosphorous-doped ZnO films grown by rf magnetron sputtering of mixed ZnO and P$_2$O$_5$ targets

with the same factor of 2000 higher UV PL than visible PL [30]. To date, the best ZnO-sapphire film we have grown had max UV PL intensity approximately 5 times the max visible PL intensity, and most films showed more intense visible emission than UV emission.

Many defects have been suggested to explain the strong visible deep-level emission. These include Zn interstitials (Zn_I), O vacancy (V_O) [31], Zn vacancy (V_{Zn}), and O substituting for Zn (O_{Zn}) [30, 32]. While the exact emission energies of these defects are still debated, a possible set of emission energies is depicted in Fig. 2.2. One group found that orange-red emission in sputtered samples corresponded to oxygen interstitials (O_I) [33]. In view of these tests, is may be worth testing growth with less oxygen in the atmosphere. On the other hand, another group grew a ZnO film with very low visible PL using MBE containing only oxygen gas in the chamber [23]. While this contradicts some other findings, it could be worthwhile to grow a film with more oxygen in the atmosphere.

3.4   Conclusions

Highly conductive ZnO films can be grown with high substrate sputter temperatures. However, the resulting carrier type remains unreliable, with most of the sputtered samples turning out *n*-type. Nitrogen was seen in many of the ZnO films, but the N source has been found and eliminated. Other possible culprits for the existing defects are either too much or too little oxygen in the chamber and other impurities in the chamber or target. The substrate lattice spacing is not likely a large factor in the deep-level PL emission.

All annealing tests increased UV PL intensity, however, annealing samples with a Zn_3As_2 layer in air led to much more deep-level visible emission. These Zn_3As_2-layer samples also became insulating and visibly damaged after annealing in air, suggesting the need to find alternative annealing methods.

3.5   Future Work

The conclusions of this work suggest many future experiments. First among these is further reproducibility testing. If the conductivity continues to vary widely between samples grown under the same conditions, then it will be very difficult to produce reliable *p*-type films.

The effects of the Zn_3As_2 layer on the ZnO film quality should be studied further. The first step would be to identify whether the Zn_3As_2 layer is crystalline at all. Next, comparing the ZnO-sapphire film with the ZnO-Zn_3As_2-sapphire film crystallinity would help us to understand the full effects. In addition, the Zn_3As_2 layer could be annealing when the substrate is heated up before sputtering. Heating it up takes about 15 min, and if it sits at 650°C for an extended time before sputtering begins, this could cause variable crystallinity in the Zn_3As_2 layer among different samples and affect the ZnO layer on top.

Other factors in the evaporation process could cause variability betweens samples. The amount of powder in the crucible, the evaporation voltage, and evaporation time may affect the Zn_3As_2 film thickness. The powder sometimes fuses into a pellet which is expelled from the crucible during evaporation; this could lead to widely-varying Zn_3As_2 film thickness, depending on when it is expelled. Lower evaporation temperatures may prevent this from happening.

Another useful study would be to test the gas flow rates. This would help us to understand whether the deep defects are caused by oxygen nonstoichiometry. Sputtering in pure O_2 or pure Ar could be useful, in addition to more combinations of gas flow rates.

Annealing in a new tube furnace will allow annealing in vacuum at temperatures above 650°C. Further, electrical performance should be characterized more thoroughly before and after annealing, which will be possible once all samples can be cut with a diamond saw and analyzed with the Hall machine.

Finding a mask that can be used at 650°C would allow direct atomic force microscopy of film edges to measure thickness. The current challenge is that Sharpie brand markers do not remove

well when heated to this high temperature, but other markers or pencils or foil could potentially make this work.

There is a nonzero possibility that the Zn_3As_2 layer could be responsible for the conductivity as discussed in Section 3.2. We would like to test that by finding a way to remove the ZnO layer without damaging the Zn_3As_2. Alternatively, we could investigate methods to remove the Zn_3As_2 after growth without damaging the ZnO, or find another method for arsenic doping that still produces p-type ZnO films without the Zn_3As_2 layer underneath.

Finally, a long-term study of the conductivity should be done. A major problem with previous p-type doping in ZnO is that it does not last over the course of months or years [8]. As these samples have only recently been grown, it remains to be seen how stable the carrier concentrations remain over the next several months or years.

Appendix A

Device Calibration

A.1   JY Horiba TRIAX 550 Spectrometer

The JY Horiba TRIAX 550 spectrometer can be calibrated using a reference light source. A low-pressure Hg pencil lamp from the BYU demo area works well. The first step is to collect the lamp light into the spectrometer. One can either focus the image of the lamp itself onto the entrance slit or shine the lamp onto a piece of paper and focus the paper image onto the entrance slit. Next, turn on and cool the photomultiplier tube (PMT) and CCD detectors. Select which of the three gratings you wish to calibrate. These gratings are blazed (work best) at different wavelengths, and may be useful for different experiments. For this work, the A grating was used since it has the best UV efficiency.

The next step is choosing a reference peak. In principle, any of the intense emission lines can be used to calibrate the spectrometer. The choice depends on where the user wants the most accurate calibration and where the detectors function. For this work, the 435.8382 nm peak was used, since both the PMT and CCD detectors work well at this wavelength, and it is near the ZnO band gap at 370 nm. Exact peak emission wavelengths can be found on the website for the National Institute of Standards and Technology (NIST); The Hg lines are reported at

https://physics.nist.gov/PhysRefData/Handbook/Tables/mercurytable2.htm.

Next, open the Hardware Configuration Utility. If it is not installed, it can be found in the "diskback/JY Horiba/Synerjy 1.8.5/Hardware Configuration Utility/" directory, copied on to the computer's main drive, and then installed from there. Run the utility. Our laboratory is using GPIB to connect to the spectrometer, meaning that the user should choose that option and then let the software automatically find the device location. After clicking start, the program will show all of the spectrometer's calibration settings currently in memory.

Start calibration by clicking "TRIAX Calibration Wizard." First enter the exact peak wavelength in nm reported by NIST that you wish to use. The spectrometer will shift to that wavelength. Now take a spectrum with the LabVIEW scan software using the PMT. Set the slits to 0.02 mm and use a step size appropriate for the grating; for grating A, this would be about 0.02 nm. Assuming that the spectrometer is not terribly miscalibrated, a 4-nm-wide scan window around the expected peak location should show the measured peak somewhere nearby.

In the utility program, enter the measured peak location. Then click "Write NOVRAM" and reinitialize the spectrometer by selecting the "Controller" menu and "Initialize" button. Reinitializing the spectrometer in this manner is very important—failing to do so will lead to bad measurements until the device is restarted.

Finally, measure the peak wavelength again with the scan program. If it is still not quite right, run the calibration wizard again and repeat the process. The user can also repeat the process for multiple gratings if desired. Moving to different wavelengths (or different gratings) and then back to the original peak allows the user to test repeatability of the calibration.

Calibrating the spectrometer at one wavelength does not guarantee that the entire spectrum will have the same accuracy. When the A grating was calibrated for this work on Feb 13, 2018, the 435.8382 nm line was repeatably accurate to within about 0.05 nm, and the 365.0153 nm line to the same margin. However, at longer wavelengths, the accuracy was lower—the 794.4555 nm line was

shifted up by about 0.2 nm, and the 1013.976 nm line shifted down by about 0.2 nm. The B grating showed very similar behavior at long wavelengths. This miscalibration of the grating turret drive cannot be fixed through this utility program, although in principle a software correction could be written in the scan program after many more measurements. For the purposes of this work, however, it is not a significant problem.

A.2   JY Synapse CCD Detector

Since most data is taken with the CCD, the user should also verify that the CCD shows a peak in the same location as the PMT. It was found here that the PMT and CCD center wavelengths matched to within about one pixel (0.037 nm) on the CCD. If the PMT and CCD do not match, the CCD calibration software (Programs - Jobin Yvon - CCD Calibration) should be used to calibrate the CCD. This software will correct the displayed CCD wavelengths without affecting the PMT wavelengths.

In addition to changing the wavelength alignment of the CCD, it may be necessary to focus the CCD. If the CCD is out of focus, all features in the spectra will be artificially widened. For example, the lines of the Hg lamp appeared about 30 px (1 nm) wide with the CCD before calibrating. After refocusing the CCD, these lines were approximately 2 px (0.07 nm) wide.

The CCD image mode, found in the main scan program CCD control panel, is an invaluable tool for focusing the CCD. The CCD is an array of pixels 1024 wide and 256 high, but regular spectral mode sums the pixels in the vertical columns and only displays the horizontal pixels, which correspond to different wavelengths. Image mode, however, displays the entire 2D array of pixels (just like a camera), so the user can see the shape of the light hitting the sensor. When the spectrometer is set to the wavelength of a prominent spectral line, image mode will show a narrow vertical line. The "select areas" button allows the user to specify a smaller region of pixels on the

CCD. This will speed up capture time, and make it easier to see small horizontal changes across pixels. In addition, pixels can be binned together to speed up capture—a 4 px or 8 px vertical bin is hardly noticeable but speeds up the acquisition by several times.

By moving the CCD very slightly in and out of the flange, the line will become wider or narrower. This line should be as narrow as possible. However, trying to slide the CCD in or out will probably also rotate the CCD slightly; this can be corrected by watching the angle of the line in image mode. The top of the line should be in the same column of pixels as the bottom of the line. When the CCD was calibrated in February 2018, the Hg lines were 1 to 2 px wide when in the center of the CCD. When they were near the edges of the CCD, they were slightly wider, meaning it is important to take spectra with narrow peaks near the center of the CCD.

Bibliography

[1] C. Klingshirn, "ZnO: Material, Physics and Applications," ChemPhysChem **8,** 782–803 (2007).

[2] "The Nobel Prize in Physics 2014,", https://www.nobelprize.org/nobel_prizes/physics/laureates/2014/, 2014, accessed: 2018-03-19.

[3] A. Ohtomo *et al.*, "Mg$_x$Zn$_{1-x}$O as a II-VI widegap semiconductor alloy," Appl. Phys. Lett. **72,** 2466 (1998).

[4] A. K. Sharma *et al.*, "Optical and structural properties of epitaxial Mg$_x$Zn$_{1-x}$O alloys," Appl. Phys. Lett. **75,** 3327 (1999).

[5] T. Makino *et al.*, "Band gap engineering based on Mg$_x$Zn$_{1-x}$O and Cd$_y$Zn$_{1-y}$O ternary alloy films," Appl. Phys. Lett. **78,** 1237 (2001).

[6] D. C. Look, "Recent advances in ZnO materials and devices," Mater. Sci. Eng. B **80,** 383–387 (2001).

[7] D. C. Look *et al.*, "Characterization of homoepitaxial p-type ZnO grown by molecular beam epitaxy," Appl. Phys. Lett. **81,** 1830–1832 (2002).

[8] T. M. Barnes, K. Olson, and C. A. Wolden, "On the formation and stability of p-type conductivity in nitrogen-doped zinc oxide," Appl. Phys. Lett. **86,** 112112 (2005).

[9] Y. R. Ryu, T. S. Lee, and H. W. White, "Properties of arsenic-doped p-type ZnO grown by hybrid beam deposition," Appl. Phys. Lett. **83,** 87–89 (2003).

[10] S. B. Zhang, S.-H. Wei, and A. Zunger, "Intrinsic n-type versus p-type doping asymmetry and the defect physics of ZnO," Phys. Rev. B **63,** 075205 (2001).

[11] S. K. Pandey *et al.*, "p-type conduction from Sb-doped ZnO thin films grown by dual ion beam sputtering in the absence of oxygen ambient," J. Appl. Phys. **114,** 163107 (2013).

[12] L. Weng *et al.*, "Characterizations of arsenic-doped zinc oxide films produced by atmospheric metal-organic chemical vapor deposition," Appl. Surf. Sci. **277,** 1–6 (2013).

[13] D. C. Look *et al.*, "As-doped p-type ZnO produced by an evaporation/sputtering process," Appl. Phys. Lett. **85,** 5269–5271 (2004).

[14] Y. Shen *et al.*, "Arsenic-doped ZnO films fabricated on silicon substrates by pulsed laser ablation," Mater. Sci. Eng. A **473,** 201–205 (2008).

[15] A. Kumar, M. Kumar, and B. P. Singh, "Fabrication and characterization of magnetron sputtered arsenic doped p-type ZnO epitaxial thin films," Appl. Surf. Sci. **256,** 7200–7203 (2010).

[16] J. C. Fan and Z. Xie, "As-doped p-type ZnO films grown on SiO2/Si by radio frequency magnetron sputtering," Appl. Surf. Sci. **254,** 6358âĂŞ–6361 (2008).

[17] J. C. Fan *et al.*, "Arsenic doped p -type zinc oxide films grown by radio frequency magnetron sputtering," J. Appl. Phys. **106,** 073709 (2009).

[18] J. C. Fan *et al.*, "Shallow acceptor and hydrogen impurity in p-type arsenic-doped ZnMgO films grown by radio frequency magnetron sputtering," Semicond. Sci. Technol. **25,** 085009 (2010).

[19] B. Cai *et al.*, "Elevated temperature dependent transport properties of phosphorus and arsenic doped zinc oxide thin films," J. Appl. Phys. **114,** 223709 (2013).

[20] S. J. Pearton, D. P. Norton, K. Ip, and Y. W. Heo, "Recent advances in processing of ZnO," J. Vac. Sci. Technol. B **22,** 932–948 (2004).

[21] S. Limpijumnong *et al.*, "Doping by Large-Size-Mismatched Impurities: The Microscopic Origin of Arsenic- or Antimony-Doped p-Type Zinc Oxide," Phys. Rev. Lett. **92,** 155504 (2004).

[22] B. Puchala and D. Morgan, "Stable interstitial dopantâĂŞvacancy complexes in ZnO," Phys. Rev. B **85,** 195207 (2012).

[23] Y. Chen *et al.*, "Plasma assisted molecular beam epitaxy of ZnO on c -plane sapphire: Growth and characterization," J. Appl. Phys. **84,** 3912 (1998).

[24] Z. Wang *et al.*, "Thermal evolution of defects in undoped zinc oxide grown by pulsed laser deposition," J. Appl. Phys. **116,** 033508 (2014).

[25] J. C. Fan *et al.*, "Dependence of conduction type of ZnO films prepared by sputtering a Zn_3As_2/ZnO target on substrate temperature and thermal treatment," J. Cryst. Growth **304,** 295–298 (2007).

[26] V. Vaithianathan, B. Lee, and S. S. Kim, "Preparation of As-doped p-type ZnO films using a Zn_3As_2/ZnO target with pulsed laser deposition," Appl. Phys. Lett. **86,** 062101 (2005).

[27] O. Bierwagen *et al.*, "Causes of incorrect carrier-type identification in van der Pauw–Hall measurements," Appl. Phys. Lett. **93,** 242108 (2008).

[28] S. W. Jung *et al.*, "Time-resolved and time-integrated photoluminescence in ZnO epilayers grown on Al_2O_3(0001) by metalorganic vapor phase epitaxy," Appl. Phys. Lett. **80,** 1924–1926 (2002).

[29] E. Przedziecka1 *et al.*, "Photoluminescence study and structural characterization of p-type ZnO doped by N and/or As acceptors," Semicond. Sci. Technol. **22,** 10–14 (2007).

[30] D. Hwang *et al.*, "Study of the photoluminescence of phosphorus-doped -type ZnO thin films grown by radio-frequency magnetron sputtering," Appl. Phys. Lett. **86,** 151917 (2005).

[31] K. Vanheusden, W. L. Warren, C. H. Seager, D. R. Tallant, and J. A. Voigt, "Mechanisms behind green photoluminescence in ZnO phosphor powders," J. Appl. Phys **79,** 7983–7990 (1996).

[32] B. Lin, Z. Fu, and Y. Jia, "Green luminescent center in undoped zinc oxide films deposited on silicon substrates," Appl. Phys. Lett. **79,** 943–945 (2001).

[33] C. H. Ahn *et al.*, "A comparative analysis of deep level emission in ZnO layers deposited by various methods," J. Appl. Phys. **105,** 013502 (2009).

Index